Volume 8
Number 17
7 May 2020
Pages 3693–3950

# Journal of Materials Chemistry B

Materials for biology and medicine

rsc.li/materials-b

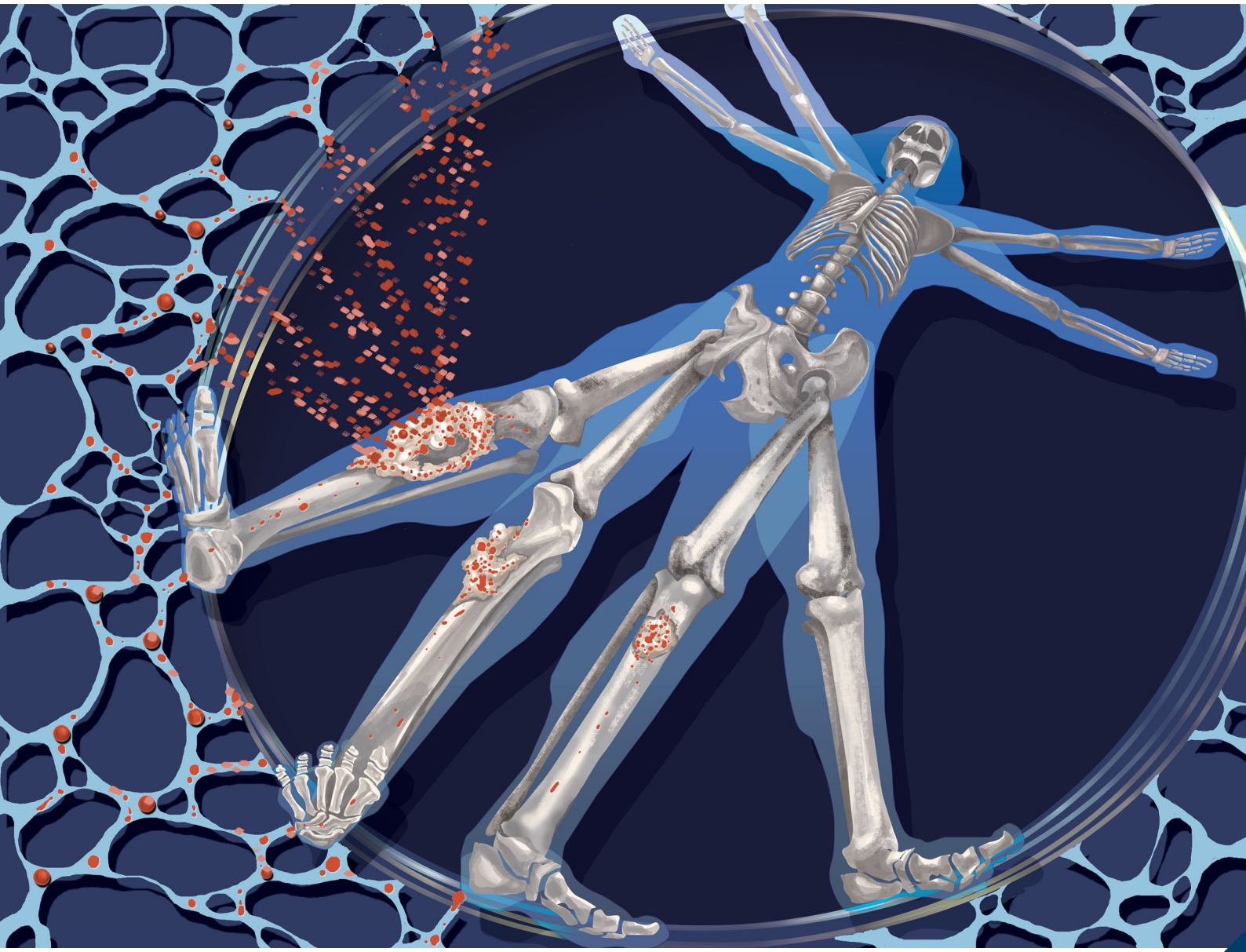

ISSN 2050-750X

ROYAL SOCIETY OF CHEMISTRY

**PAPER**

Wen-Hsuan Chiang, Hsin-Cheng Chiu *et al.*
Alendronate/folic acid-decorated polymeric nanoparticles for hierarchically targetable chemotherapy against bone metastatic breast cancer

Indexed in Medline!

Journal of Materials Chemistry B

ROYAL SOCIETY OF CHEMISTRY

PAPER

View Article Online
View Journal | View Issue





Cite this: *J. Mater. Chem. B*, 2020, **8**, 3789

# Alendronate/folic acid-decorated polymeric nanoparticles for hierarchically targetable chemotherapy against bone metastatic breast cancer†

Shih-Hong Chen,‡[abc] Te-I Liu,‡[a] Cheng-Lin Chuang,[a] Hsin-Hung Chen,[d] Wen-Hsuan Chiang *[d] and Hsin-Cheng Chiu *[a]

Received 7th January 2020,
Accepted 23rd February 2020

DOI: 10.1039/d0tb00046a

rsc.li/materials-b

To considerably enhance treatment efficacy for bone metastatic breast cancer *via* dual bone/tumor-targeted chemotherapy, a nanoparticle-based delivery system comprising poly(lactic-*co*-glycolic acid) (PLGA) as the hydrophobic core coated with alendronate-modified D-α-tocopheryl polyethylene glycol succinate (ALN-TPGS) and folic acid-conjugated TPGS (FA-TPGS) was developed as a vehicle for paclitaxel (PTX) in this work. The ALN/FA-decorated nanoparticles not only showed superior ALN-mediated binding affinity for hydroxyapatite abundant in bone tissue but also promoted uptake of payloads by folate receptor-overexpressing cancer cells to significantly augment PTX cytotoxicity. Notably, through dual-targetable delivery to the bone matrix and folate receptor-overexpressing 4T1 tumors, the PTX-loaded nanoparticles substantially accumulated in bone metastases *in vivo* and inhibited 4T1 tumor growth and lung metastasis, leading to significant improvement of the survival rate of treated mice. Upon treatment with the ALN/FA-decorated PTX-loaded nanoparticles, the bone destruction and bone loss of the tumor-bearing mice were appreciably retarded, and the adverse effects on normal tissues were alleviated. These results demonstrate that the ALN/FA-decorated PTX-loaded delivery system developed in this study shows great promise for the effective treatment of bone metastatic breast cancer.

## 1. Introduction

The skeleton is one of the most common organs to be invaded by metastatic cancers due to its physiological environment.[1–3] Among different cancers, breast cancer displays a relatively high incidence of bone metastasis.[4–6] More than 80% of women who die from breast cancer have evidence of bone metastasis.[7] Bone metastases cause a series of skeleton-related complications, including bone pain, pathological fracture, hypercalcemia and nerve compression, thus shorting survival time and reducing quality of life for patients.[8–10] Unfortunately, multiple metastatic nodules cannot be completely eliminated by clinical radiation or surgical therapy, which limits treatment efficacy for bone metastasis.[9,10] In this regard, chemotherapy has emerged as a promising approach to treat bone metastasis. To overcome the drawbacks of conventional chemotherapy, such as nonspecific tumor targeting, severe side effects and poor permeability in bone tissue, it is essential to develop active bone-targeted drug delivery systems (DDSs).

Taking advantage of the high content of hydroxyapatite (HA) in the bone matrix and tissue-specific cells, several HA-binding molecules, such as bisphosphonates (BPs), tetracyclines and acidic oligopeptides, have been conjugated with various nanoparticle-based DDSs for efficient bone-targeted drug transport.[2,5,10–18] Among them, alendronate (ALN), a third-generation BP, is a superior bone-targeting ligand because its binding affinity for tumor-invaded bone is 10–20 times higher than that for healthy bone tissue.[5,10] Zhu and co-workers synthesized the ALN-decorated amphiphilic hyperbranched copolymer composed of a hydrophobic hyperbranched Boltorn H40 (H40) core conjugated with ALN targeting moiety and hydrophilic poly(ethylene glycol) (PEG) arms. The polymeric micelles from the self-assembly of H40-*star*-PEG/ALN were used as a carrier of doxorubicin (DOX) for bone-targeted drug delivery. The *in vitro* studies showed that the H40-*star*-PEG/ALN micelles rapidly

[a] *Department of Biomedical Engineering and Environmental Sciences, National Tsing Hua University, Hsinchu 30013, Taiwan. E-mail: hscchiu@mx.nthu.edu.tw*
[b] *Department of Anesthesiology, Taipei Tzu Chi Hospital, New Taipei City 231, Taiwan*
[c] *Department of Anesthesiology, National Taiwan University Hospital Hsin-Chu Branch, Hsinchu, Taiwan*
[d] *Department of Chemical Engineering, National Chung Hsing University, Taichung 402, Taiwan. E-mail: whchiang@dragon.nchu.edu.tw*

† Electronic supplementary information (ESI) available. See DOI: 10.1039/d0tb00046a

‡ These authors contributed equally to this work.

bound to HA and the DOX-loaded H40-*star*-PEG/ALN micelles efficiently killed HN-6 cancer cells.[19] As reported by Swami *et al.*, bortezomib-loaded nanoparticles consisting of poly(D,L-lactic-*co*-glycolic acid)-*b*-PEG (PLGA-*b*-PEG) and ALN-conjugated PLGA-*b*-PEG showed considerably increased survival and decreased tumor progression in multiple myeloma-bearing mice *via* outstanding bone-homing ability.[14] Moreover, Zhao's group developed PEG/ALN-coated nanoparticles made of a $Zn^{2+}$ coordination polymer as a cisplatin prodrug (DSP) carrier. Through their small size (~55 nm) and high affinity for bone, the DSP-Zn@PEG-ALN nanoparticles efficiently delivered cisplatin to bone metastatic lesions, thus significantly enhancing therapeutic efficacy for treating bone metastasis, including tumor inhibition, pain relief, and reduced bone destruction.[5] To achieve bone-targeted gene delivery for the expression of stromal cell-derived factor 1 (SDF-1), ALN-modified liposomal nanoparticles (Aln-Lipo) were developed as a gene carrier by Chen *et al.*[16] These nanoparticles displayed a strong binding ability to HA and boosted SDF-1 transfection in osteoblastic cells. Systemic infusion of Aln-Lipo-SDF-1 appreciably increased the deposition of SDF-1 in osseous tissue, followed by the attraction of transplanted mesenchymal stem cells to participate in bone regeneration.[16]

Although the aforementioned nanocarriers equipped with bone-targeting ligands could promote the accumulation of therapeutic agents in the bone structure to some extent, these DDSs may not be effective in targeting cancer cells at bone metastatic sites. This is because these bone-targeting DDSs are mostly directed to the bone tissue but not the cancer cells within it. Taking these facts into consideration, it is thus necessary to further engineer the bone-targeted nanoscaled DDSs with additional biological ligands or antibodies for the effective delivery of drugs to specific cancer cells in bone lesion regions. To this end, some new strategies have been proposed.[20–23] For example, Wu's group developed bone- and CD44-dual-targeted redox-sensitive liposomes to treat orthotopic osteosarcoma.[20] In their study, the modification of hyaluronic acid with ALN did not reduce its CD44 binding affinity but did facilitate accumulation of the liposomes at the orthotopic lesion site. The preclinical study demonstrated that the liposomes showed great ability to achieve specific intracellular drug delivery to orthotopic osteosarcoma and reduce mortality in the animals. Zhao *et al.* have developed polymeric nanoparticles from self-assembly of phenylboronic acid and folate grafted chitosan as a smart carrier of DOX, featured with dual pH/glucose concentration-triggered DOX release and enhanced cellular uptake by cancer cells *via* folate receptor (FAR) mediated endocytosis.[24] On the other hand, in view of that the folate receptor is overexpressed on the surface of several cancers, including breast, kidney, lung, brain, and ovary cancers for improved delivery of DOX to folate receptor-positive breast cancer cells in bone metastases, Ke *et al.* designed dual-targeted liposomes as drug carriers by incorporating a bone-homing octapeptide with eight repeating sequences of aspartate (Asp8) and folate onto the liposome surfaces. The therapeutic liposomes relieved pain and enhanced survival in mice bearing folate receptor-overexpressing MDA-MB-231 tumors *via* dual-targeted effects.[21]

To greatly increase the efficacy of chemotherapy in bone metastatic breast cancer, in this study, a practical strategy was developed to fabricate dual bone/tumor-targeted nanoparticles capable of effectively delivering a chemotherapy drug, paclitaxel (PTX), to bone metastatic breast cancer (Scheme 1). First, ALN-modified D-α-tocopheryl polyethylene glycol 1000 succinate (TPGS) (ALN-TPGS) and folic acid-conjugated TPGS (FA-TPGS) were prepared by conjugating TPGS with ALN and FA, respectively. The ALN/FA-decorated PTX-loaded nanoparticles were then obtained by coating both ALN-TPGS and FA-TPGS on the surfaces of drug-loaded poly(lactic-*co*-glycolic acid) (PLGA) nanoparticles upon the hydrophobic anchoring of the vitamin E moiety of TPGS. In addition to the physicochemical characterization and *in vitro* drug release study of ALN/FA-decorated PTX-loaded nanoparticles, the HA-binding ability of the nanoparticles was further evaluated. The *in vitro*

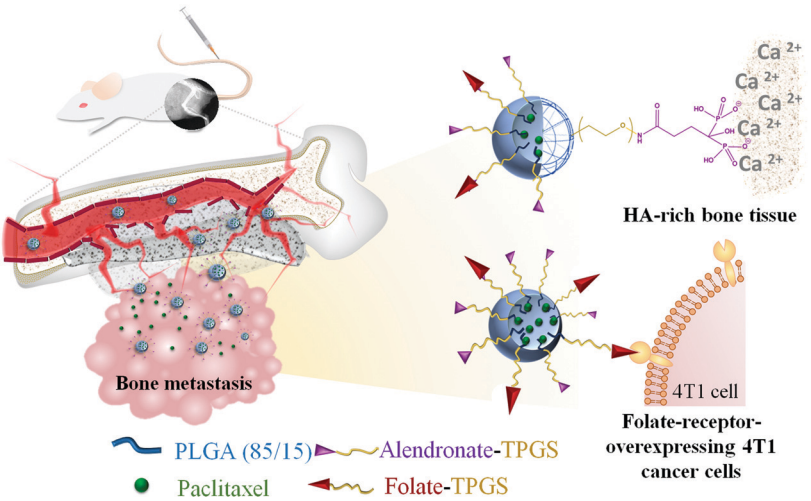


Scheme 1 Illustration of the development of ALN/FA-decorated PTX-loaded nanoparticles for dual-targeted chemotherapy for bone metastatic breast cancer.

 

cellular uptake of dual-targeted PTX-loaded nanoparticles and their cytotoxicity against the murine mammary carcinoma cell line 4T1 with folate receptor overexpression were assessed. To demonstrate the feasibility of ALN/FA-decorated PTX-loaded polymeric nanoparticles for treating bone metastatic breast cancer, extensive studies of *in vivo* biodistribution, tumor growth inhibition and systemic toxicity were conducted in this work.

## 2. Experimental section

### 2.1. Materials

PLGA (LA/GA 85/15, I.V. 0.42 dL $g^{-1}$, hydroxyl terminated) was acquired from Green Square (Taiwan). Succinic anhydride (SA), TPGS, 1-(3-dimethylaminopropyl)-3-ethylcarbodiimide hydrochloride (EDC), rhodamine b (Rho), FA, 3-(4,5-dimethylthiazol-2-yl)-2,5-diphenyltetrazolium bromide (MTT), 1,1′-dioctadecyl-3,3,3′,3′-tetramethylindocarbocyanine perchlorate (DiI) and 3,3′-dioctadecyloxacarbocyanine perchlorate (DiO) were supplied by Sigma-Aldrich (USA). *N*-Hydroxysuccinimide (NHS), 4-dimethylaminopyridine (DMAP) and *N*,*N*′-dicyclohexylcarbodiimide (DCC) were purchased from Alfa Aesar (USA). ALN was purchased from Tokyo Chemical Industry (Japan). PTX was obtained from LC Laboratories (USA). Deionized water was produced from Milli-Q Synthesis (18 MΩ, Millipore). All other chemicals were reagent grade and used as received. For cell culture studies, Dulbecco's modified Eagle's medium (DMEM), RPMI 1640 medium, fetal bovine serum (FBS), 0.25% trypsin–EDTA solution, penicillin–streptomycin solution and Hoechst 33342 were purchased from Thermo Fisher Scientific (Waltham, MA, USA). 4T1 (murine mammary carcinoma cell line), CT26 (murine colon adenocarcinoma cell line) and A549 (human lung adenocarcinoma cell line) cells were obtained from Food Industry Research and Development Institute (Hsinchu City, Taiwan). Five-week-old BALB/C female mice were purchased from the National Laboratory Animal Center, Taiwan. The use of laboratory animal was approved by the Institutional Animal Care and Use Committee (IACUC) of National Tsing Hua University, Taiwan (approved number: IACUC 10343). Approved guidelines for the care and use of laboratory animals from IACUC were followed throughout the study.

### 2.2. Synthesis of SA-activated TPGS

TPGS (0.25 g, 0.16 mmol), SA (33 mg, 0.32 mmol) and DMAP (39 mg, 0.32 mmol) were dissolved in chloroform (3.0 mL). The reaction was performed with stirring at room temperature for 24 h, followed by rotary evaporation to eliminate the solvent. The product was redissolved in deionized water and then dialyzed (Cellu Sep MWCO 1000) against deionized water for 3 days to remove the residual SA and DMAP. The final product was collected by lyophilization and characterized by $^1$H-NMR (500 MHz, Bruker Avance 500 NMR).

### 2.3. Synthesis of ALN-TPGS

The ALN-TPGS employed in this work was synthesized by EDC/NHS-mediated aminolysis of SA-activated TPGS with ALN molecules, as presented in Fig. S1 (ESI†). In brief, SA-activated TPGS, EDC and NHS (10-fold molar excess with respect to SA-activated TPGS) were dissolved in dry dioxane containing triethylamine as the catalyst, and the reaction was performed at 30 °C for 8 h. A prescribed amount of ALN (10-fold excess with respect to SA-activated TPGS) in deionized water was added to the above solution, and the reaction was carried out for an additional 4 h. Subsequently, the solution was dialyzed (Cellu Sep MWCO 1000) against deionized water to eliminate solvent and unreacted ALN. The final product was collected by lyophilization and characterized by FT-IR (Thermo Scientific Nicolet 6700, USA) and ICP-MS (Element™ Series HR-ICP-MS, Thermo Fisher Scientific Inc., USA).

### 2.4. Synthesis of FA-TPGS

The detailed synthetic route of FA-TPGS is described in Fig. S2 (ESI†). In brief, TPGS (2 g, 1.3 mmol), FA in 5-fold molar excess with respect to TPGS, DCC (in 8-fold molar excess) and DMAP (equimolar) were dissolved in anhydrous DMSO (10.0 mL). The reaction was carried out with stirring at 40 °C for 5 days, followed by repeated filtration to remove the byproduct dicyclohexylcarbodiurea (DCU). The solution was then dialyzed (Cellu Sep MWCO 1000) against DMSO for 3 days to eliminate the residual DCU, unreacted FA and DMAP, followed by dialysis against deionized water for 3 days to remove DMSO. The final product was collected by lyophilization, and the structure was characterized by a UV/Vis spectrophotometer (U2900, Hitachi, Japan) and by $^1$H-NMR.

### 2.5. Preparation of nanoparticles

Various PTX-loaded nanoparticles coated with either pristine TPGS or TPGS adducts were prepared by the single emulsion approach. The ALN-TPGS/FA-TPGS/PLGA nanoparticles (AFTPNs) loaded with PTX were obtained as follows. PLGA (5.0 mg), ALN-TPGS (1.6 mg), FA-TPGS (2.4 mg) and PTX (0.5 mg) dissolved in chloroform (0.3 mL) were added to pH 7.4 phosphate buffer (10 mM, 3.5 mL). In an ice water bath, the solution was emulsified for 7 min (ultrasonic processor, 20 kHz, 750 W), followed by rotary evaporation to remove chloroform. The solution containing PTX-loaded AFTPNs was dialyzed (Cellu Sep MWCO 600–8000) against 10 mM pH 7.4 phosphate buffer at 4 °C for 1 day, followed by passage through a 0.45 μm filter to remove the unloaded PTX. For comparison, PTX-loaded AFTPNs with different weight ratios (A/F ratio) of ALN-TPGS and FA-TPGS in feed, PTX-loaded ALN-TPGS/PLGA nanoparticles (ATPNs), PTX-loaded FA-TPGS/PLGA nanoparticles (FTPNs), and PTX-loaded TPGS/PLGA nanoparticles (TPNs) were prepared in a similar manner. In addition, by using Rho-conjugated PLGA instead of PLGA, the Rho-labeled nanoparticles coated with either TPGS or TPGS adducts employed in the HA binding test and *in vitro* cellular uptake study were prepared according to the aforementioned method. The synthetic route of Rho-conjugated PLGA is presented in Fig. S3 (ESI†).

### 2.6. Characterization of nanoparticles

The particle size, size distribution and zeta potential of PTX-carrying nanoparticles in aqueous solutions were measured by dynamic light scattering (DLS) using a ZetaSizer Nano Series instrument (Malvern Instruments, U.K.). The data shown herein

represent an average of at least triplicate measurements. The morphology of PTX-free and PTX-loaded ATPNs after negative staining with uranyl acetate was observed by TEM (JEOL JEM-2100F, Japan).

Agilent 1100 high-performance liquid chromatography (HPLC) with a reversed-phase C18 column was utilized to determine the drug-loading efficiency and content of various PTX-loaded nanoparticles. First, 100 μL of PTX-loaded nanoparticle solution was lyophilized and then dissolved in acetonitrile, followed by ultrasonication for 10 min to ensure that PTX was completely dissolved in acetonitrile. The solution was passed through a 0.45 μm filter, and the PTX content was determined by HPLC. The mobile phase consisted of acetonitrile, water and methanol (1 : 1 : 1, v/v/v) with a gradient elution pumped at a flow rate of 1.0 mL $min^{-1}$, and the column was maintained at 30 °C. The absorbance of PTX at 227 nm was determined. The drug-loading efficiency (DLE) and loading content (DLC) were calculated by the following formulas:

$$\text{DLE (\%)} = (\text{weight of PTX loaded/weight of PTX in feed}) \times 100\%.$$

$$\text{DLC (\%)} = (\text{weight of PTX loaded/total weight of PTX-loaded nanoparticles}) \times 100\%.$$

For *in vitro* drug release measurement, the PTX-loaded nanoparticle solution (0.2 mL) was dialyzed (Cellu Sep MWCO 6000–8000) against PBS (pH 7.4, 20 mL) containing 0.2% (w/v) Tween 80 at 37 °C. The internal sample was withdrawn periodically, and the content of PTX was determined by HPLC as described above.

### 2.7. HA binding test

The binding affinity of various Rho-labeled nanoparticles for bone minerals was evaluated as reported elsewhere.[25,26] In brief, various Rho-labeled nanoparticles (3.0 mg $mL^{-1}$) were dispersed in 5 mL of PBS in centrifugal tubes containing 50 mg of HA microparticles. The mixed solutions were gently shaken at 100 rpm at 37 °C. At the prescribed time intervals, the mixtures were centrifuged at 4000*g* for 5 min, and the Rho fluorescence of the supernatant in the 570–650 nm range was measured by a fluorescence spectrometer (F-7000, Hitachi, Japan). The binding capability for HA was calculated according to the following formula:

$$\text{HA binding (\%)} = ((\text{Initial Rho fluorescence intensity} - \text{Rho fluorescence intensity at the predetermined time points})/\text{Initial Rho fluorescence intensity}) \times 100\%.$$

After centrifugation of the above samples, fluorescence images of the collected HA microparticles were obtained using a Nikon ECLIPSE Ti-U inverted microscope (Japan).

### 2.8. *In vitro* cellular uptake study

FA receptor-overexpressing 4T1 breast carcinoma cells ($3 \times 10^5$ cells per well) seeded onto 22 mm round glass coverslips in 6-well plates were incubated separately with Rho-labeled TPNs, ATPNs, FTPNs and AFTPNs (Rho concentration = 10 μM) at 37 °C for 30 min. After two washes with PBS and immobilization with 4% formaldehyde, the cell nucleus was stained with Hoechst 33342 for 15 min. The cellular images were obtained using a laser scanning confocal microscope (LSCM) system (Zeiss LSM780, Germany) equipped with a Hoechst set (Ex. 405 nm and Em. 410–492 nm) and a Rho set (Ex. 488 nm and Em. 550–650 nm). On the other hand, DiO, as a fluorescent dye, was encapsulated into various nanoparticles coated with TPGS or TPGS adducts. To further explore the effects of the surface-coated FA-TPGS on the cellular uptake of PLGA-based nanoparticles, 4T1 cells and folic acid-pretreated 4T1 cells ($3 \times 10^5$ cells per well) seeded in 6-well culture plates were incubated with DiO-loaded TPN, FTPN, ATPN and AFTPN solutions (DiO concentration = 10 μM), respectively, at 37 °C for 1 h. After being washed three times with PBS, DMSO was then added to each well for cell lysis. The DiO fluorescence at 500–650 nm was determined with a fluorescence spectrometer (F-7000, Hitachi, Japan). For comparison, CT26 colon cancer cells with folate receptor overexpression and A549 lung carcinoma cells with low folate receptor expression were individually incubated with various DiO-loaded nanoparticles, and the DiO fluorescence was determined in the aforementioned manner.

### 2.9. *In vitro* cytotoxicity examination

In this study, cell viability was examined by MTT assay. First, 4T1 cells ($5 \times 10^3$ cells per well) were seeded in a 96-well plate and incubated in 0.2 mL of RPMI containing 10% FBS and 1% penicillin at 37 °C for 24 h in an atmosphere of 5% $CO_2$. The spent medium was then replaced with 100 μL of fresh medium containing free PTX, various PTX-loaded nanoparticles at varying PTX concentrations, or PTX-free nanoparticles, and the cells were further incubated for 8 h. After being washed twice with PBS, the cells were reincubated for another 24 h. The MTT solution (10 μL, 5.0 mg $mL^{-1}$) was then added into each well, followed by incubation at 37 °C for 3 h. After discarding the culture medium, DMSO (200 μL) was added to dissolve the precipitate, and the absorbance at 570 nm was determined by a microplate reader (FLUOstar, OPTIMA, BGM Labtech, Germany).

### 2.10. Animals and tumor model

A mouse model of bone metastasis from breast cancer was established by intratibial injection of 4T1 cells, as reported previously, with slight modification.[5,15] In brief, with the mice (BALB/C, female) anesthetized with isoflurane, the tibia of the right hind limb was injected with $2 \times 10^6$ 4T1 cells using a 25-gauge needle. The mice were placed in the animal room and were given free access to food and water throughout the experiment. Tumor volume ($V$) was calculated as follows: $V = L \times W^2/2$, where $W$ is the tumor measurement at the widest point and $L$ is the tumor dimension at the longest point.

### 2.11. *In vivo* biodistribution

The 4T1 tumor-bearing mice were intravenously injected with PBS or various DiI-loaded nanoparticles *via* the tail vein at a prescribed DiI dosage (0.1 μg $\mu L^{-1}$). The treated mice were sacrificed at 8 h post injection, and the major organs, including

 

the heart, the liver, the spleen, the lung, the kidney, healthy bone and bone metastatic lesions, were harvested. DiI fluorescence images of individual organs (Ex. 535 nm and Em. 660 nm) were collected using the IVIS (Xenogen IVIS Spectrum).

### 2.12. *In vivo* tumor growth inhibition

Mice with a tumor size of $\sim$50 mm$^3$ were randomly divided into 5 groups (5 in each group) and intravenously injected with PBS, PTX-loaded TPNs, PTX-loaded FTPNs, PTX-loaded ATPNs or AFTPNs at a PTX dosage of 7.5 mg kg$^{-1}$. Each group was treated with a total of three doses at days 0, 3 and 6. The tumor size and body weight were monitored regularly to evaluate the antitumor efficacy. Moreover, the survival rates of mice treated with different formulations were assessed. Sections of major organs (heart, liver, spleen, lung and kidney) were H&E stained and observed by an Olympus IX70 inverted microscope (Japan).

### 2.13. Three-dimensional (3D) micro-computed tomography (micro-CT) reconstruction of tibias

*Ex vivo* micro-CT analysis of mouse leg bones was conducted to evaluate the bone damage. The tumor-bearing hind legs were dissected from the sacrificed mice and stored in 4% paraformaldehyde solution. The legs were placed in a scanning holder and analyzed using a SKYSCAN 1076 Micro-CT (National Laboratory Animal Center, Taipei, Taiwan). After scanning, 3D models were reconstructed and evaluated using SKYSCAN 1076 Micro-CT software. In addition, bone mineral density (BMD) was calculated automatically using the software.

### 2.14. Systemic toxicity evaluation

The systemic toxicity of various PTX-loaded nanoparticles in the treated tumor-bearing mice was assessed by determining the levels of alkaline phosphatase (ALP) and aspartate aminotransferase (ALT). Blood (0.1 mL) withdrawn from the orbital sinus of the treated mice at day 14 after the first therapeutic treatment was mixed with lithium heparin, and the sample was analyzed for ALP and ALT on a Clinical Analyzer AmiShield VCA-TC-100 (ProtectLife International Biomedical Inc.).

### 2.15. Statistical analysis

All data are reported as the mean $\pm$ standard deviation (SD). Student's *t*-test was used to analyze the differences between the control and test groups. Statistical significance is indicated as (n.s.) $P > 0.05$, (*) $P < 0.05$, (**) $P < 0.01$ and (***) $P < 0.001$.

## 3. Results and discussion

### 3.1. Synthesis and characterization of ALN-TPGS and FA-TPGS

As shown in the $^1$H-NMR spectrum of SA-activated TPGS (Fig. S4, ESI†), from the integral ratio of the feature proton signals of the ethyl group ($\delta$ 2.6 ppm) of SA and the methyl groups ($\delta$ 0.81 ppm) of TPGS, a high conjugation efficiency (87.6%) of TPGS with SA was obtained. The ALN-TPGS adduct employed in this work was prepared by the EDC/NHS-mediated aminolysis of SA-activated TPGS with ALN. With ALN conjugated to SA-activated TPGS, as presented in Fig. S5a (ESI†), the FT-IR spectrum of ALN-TPGS showed the characteristic absorption bands at 3348 cm$^{-1}$ and 1652 cm$^{-1}$, ascribed to the O–H stretching vibration of ALN and the C=O stretching vibration of the secondary amide, respectively, which were absent in the SA-activated TPGS. Additionally, the feature phosphorus peak of the bisphosphate group at $\delta$ 18.94 ppm was observed in the $^{31}$P-NMR spectrum of ALN-TPGS (Fig. S6, ESI†). The above results are indicative of the successful conjugation of SA-activated TPGS and ALN. Moreover, based on the phosphorus content of ALN-TPGS quantitatively analyzed by ICP-MS, the coupling efficiency was determined to be $\sim$55%. On the other hand, through the DCC/DMAP-mediated esterification of TPGS with FA, FA-TPGS was obtained. The UV absorbance (285 nm) from the FA residues of FA-TPGS in the UV spectrum confirms the successful modification of TPGS with FA (Fig. S7, ESI†). As presented in the $^1$H-NMR spectrum of FA-TPGS (Fig. S5b, ESI†), according to the integral ratio of the feature proton signals of the benzene ring ($\delta$ 7.61 ppm) of FA and the methyl groups ($\delta$ 0.81 ppm) of TPGS, the conjugation efficiency was estimated to be $\sim$52%.

### 3.2. Preparation and characterization of PTX-loaded PLGA-based nanoparticles

Using a simple emulsion approach, various PTX-carrying PLGA-based nanoparticles coated with either TPGS or its adducts *via* the hydrophobic attachment of vitamin E moieties were obtained. The resulting PTX-TPNs and PTX-FTPNs exhibited similar mean hydrodynamic diameters ($D_h$) of $\sim$140 nm and monomodal size distributions in aqueous solution (pH 7.4) (Fig. 1a and Table 1). The monodispersity of various NPs was further confirmed by the DLS number-based size distribution and raw correlation data (Fig. S8, ESI†). Compared to PTX-TPNs and PTX-FTPNs, PTX-ATPNs showed somewhat smaller particle sizes ($D_h$ *ca.* 120 nm) and appreciably higher zeta potential (−42.2 mV). This indicates that coating of ALN-TPGS on PLGA nanoparticle surfaces rendered the colloidal surfaces remarkably negatively charged due to the bisphosphate groups of ALN residues. Furthermore, for PTX-AFTPNs, as the weight ratio (A/F ratio) of ALN-TPGS and FA-TPGS in the feed was adjusted from 0.25 to 4.0, the zeta potential was appreciably increased from −25.1 to −38.7 mV, while the particle size was slightly reduced (Table 1). The transmission electron microscopy (TEM) images further revealed that the PTX-ATPNs were well-dispersed and spherical (Fig. S8, ESI†).

As shown in Fig. 1b and c, the particle sizes of various PTX-loaded nanoparticles in PBS and DMEM at 37 °C remained largely stable over 7 days, indicating that the amphiphilic TPGS and its adducts were capable of anchoring with the hydrophobic vitamin E moieties in PLGA particles and with the PEG chain segments to stabilize the nanoparticles in aqueous phase. Moreover, by the encapsulation of poorly water-soluble PTX molecules into hydrophobic PLGA cores, the resulting PTX-loaded nanoparticles coated with TPGS or its adduct displayed satisfactory DLE and content (Table 1). Notably, a significant reduction in the initial burst release (below 25%) of PTX from cargo-loaded nanoparticles in PBS at 37 °C within 6 h was

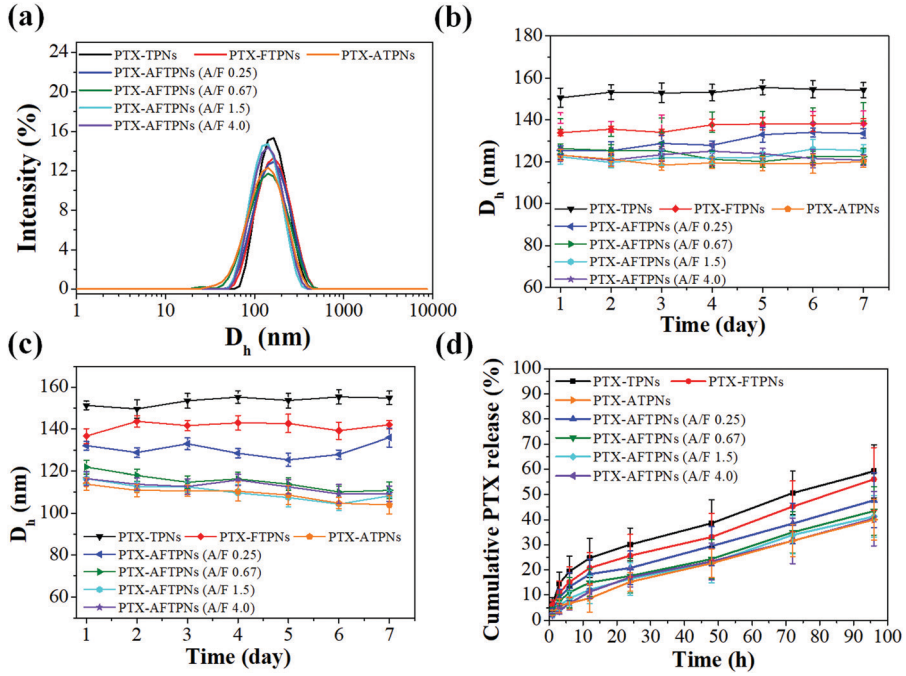


Fig. 1 (a) DLS particle size distribution profiles of various PTX-loaded nanoparticles in an aqueous solution with pH 7.4. (b) Colloidal stability of various PTX-loaded nanoparticles in PBS at 37 °C. (c) Colloidal stability of various PTX-loaded nanoparticles in DMEM at 37 °C. (d) Cumulative PTX release profiles of various PTX-loaded nanoparticles in PBS at 37 °C.

Table 1 DLS data and drug-loading characterization of PTX-loaded nanoparticles

| | | | | PTX loading | |
|---|---|---|---|---|---|
| Sample | $D_h$[a] (nm) | PDI | Zeta potential (mV) | Efficiency (%) | Content (wt%) |
| PTX-TPNs | 150.3 ± 2.13[b] | 0.111 | −25.4 ± 1.21 | 78.2 ± 2.62 | 4.2 ± 0.02 |
| PTX-FTPNs | 140.2 ± 4.81 | 0.195 | −18.1 ± 0.91 | 68.5 ± 5.49 | 3.61 ± 0.29 |
| PTX-AFTPNs (A/F 0.25) | 131.3 ± 3.53 | 0.191 | −25.1 ± 1.15 | 70.4 ± 3.53 | 3.71 ± 0.19 |
| PTX-AFTPNs (A/F 0.67) | 125.9 ± 0.95 | 0.189 | −29.6 ± 1.21 | 71.8 ± 3.96 | 3.78 ± 0.21 |
| PTX-AFTPNs (A/F 1.5) | 120.4 ± 1.81 | 0.142 | −31.1 ± 1.01 | 72.1 ± 5.71 | 3.79 ± 0.31 |
| PTX-AFTPNs (A/F 4.0) | 122.9 ± 1.65 | 0.169 | −38.7 ± 2.71 | 70.8 ± 1.38 | 3.73 ± 0.07 |
| PTX-ATPNs | 121.0 ± 0.63 | 0.174 | −42.2 ± 0.89 | 90.7 ± 6.86 | 4.87 ± 0.56 |

[a] DLS measurement was performed in phosphate buffer (pH 7.4, I 0.1 M) at 25 °C. [b] Error bars represent the mean ± s.d. ($n \geq 10$).

observed (Fig. 1d), signifying that the solid PLGA cores combined with TPGS-based surface coating could appreciably retard PTX leakage by the hydrophobic interaction and π–π aromatic stacking. Interestingly, for PTX-AFTPNs, with the content of ALN-TPGS coated on the surfaces of PTX-containing PLGA nanoparticles increasing, PTX liberation was further reduced. Considering that ALN-TPGS is more hydrophilic than FA-TPGS and TPGS because of the presence of its anionic bisphosphate group, it was assumed that during the single emulsion process, most of the ALN-TPGS segments were apt to reside on the surfaces of hydrophobic PLGA cores, whereas some of the FA-TPGS and TPGS segments were embedded in the PLGA cores, leading to the formation of a porous core structure to accelerate payload outflow. Similar studies reporting TPGS molecules as pore-forming agents to promote drug release of PLGA-based DDSs have also been published.[27,28]

### 3.3. HA binding assessment

The lack of drug targeting has been the main hurdle in treating bone metastasis and often causes undesired severe damage in normal tissues.[29] In view of the strong affinity of ALN for HA, which is abundant in the regions of bone metastatic lesions, various ALN-conjugated nanoparticle-based DDSs have been designed for bone-targeted delivery of therapeutic agents.[2,4,5,13,14] In this work, to assess the binding capability of the developed ATPNs and AFTPNs with bone tissues by the HA binding assay, the Rho-labeled nanoparticles were mixed with HA in PBS. At different time intervals, the Rho fluorescence intensity of the supernatants and HA microparticles separated from mixed solutions was determined. According to the Rho fluorescence spectra of the supernatants (Fig. S13, ESI†), the HA binding (%) of these nanoparticles at each indicated time was calculated by the formula as described in Experimental section – HA binding test. As presented in Fig. S8a (ESI†), the HA binding (~53%) of

 

Rho-labeled ATPNs mixed with HA for 3 h was substantially superior to that (less than 13%) of Rho-labeled TPNs and FTPNs (Rho-TPNs and Rho-FTPNs). With the reaction time being prolonged to 24 h, a continuous increase in HA binding for Rho-ATPNs and Rho-AFTPNs (with the A/F ratio equal to or beyond 0.67) was observed. The fluorescence images also show that the HA pellets incubated with either Rho-ATPNs or Rho-AFTPNs (A/F ratio above 0.67) exhibited a remarkably increased Rho fluorescence intensity compared to their counterparts treated with Rho-TPNs or Rho-FTPNs, as shown in Fig. S8b and c (ESI†). Notably, after a 12 h reaction, the Rho fluorescence signals of HA microparticles treated with the former two were ~10-fold higher than those of HA microparticles mixed with the latter two (Fig. S8c, ESI†). Nevertheless, it is worth mentioning that the AFTPNs with an A/F ratio of 0.25 showed a significantly reduced HA binding affinity (Fig. S8, ESI†). These results strongly demonstrate that adequate coating of ALN-TPGS on the surfaces of PLGA cores can endow the nanoparticles with outstanding bone-targeting capability, which is a critical prerequisite for penetration into the bone metastatic region *in vivo*.

### 3.4. *In vitro* cellular uptake

The effect of surface coating with FA-TPGS segments on the cellular uptake of the FTPNs and AFTPNs was explored using folate receptor-overexpressing 4T1 cells as a model cancer cell line. As observed in the LSCM images (Fig. 2a), murine mammary carcinoma 4T1 cells incubated with either the Rho-FTPNs or Rho-AFTPNs at 37 °C for 1 h exhibited much stronger fluorescence signals in the cytoplasm than did the Rho-TPN- or Rho-ATPN-treated cells. Additionally, a significantly enhanced mean fluorescence intensity of 4T1 cells incubated with DiO-carrying FTPNs or AFTPNs (DiO concentration = 10 μM) compared to that of cells treated with DiO-loaded ATPNs and TPNs was obtained (Fig. 2b). Notably, the uptake of DiO-loaded FTPNs and AFTPNs by 4T1 cells pretreated with free FA (2.0 μM) was largely inhibited, as reflected by the remarkably reduced DiO fluorescence intensity of 4T1 cells. By contrast, the internalization of DiO-loaded nanoparticles without FA decoration (ATPNs and TPNs) by the folic acid-pretreated 4T1 cells was not substantially different (Fig. 2b). These findings clearly confirm that the enhanced cellular uptake of the FTPNs and AFTPNs by 4T1 cells occurred *via* folate receptor-mediated endocytosis. Although the cellular uptake was reduced to some extent with a reduced content of FA-TPGS on the surfaces of AFTPNs, the AFTPNs with an A/F ratio in the range 0.25–1.5 still showed a good ability of the FA residues to initiate receptor-mediated endocytosis compared to those without FA-TPGS, as illustrated in Fig. 2a and b. Similar results were also observed with folate receptor-overexpressing murine colon adenocarcinoma CT-26 cancer cells (Fig. S12, ESI†). By contrast, no significant difference was observed in the uptake of various DiO-labeled nanoparticles by human lung adenocarcinoma A549 cells, which are characterized by low expression of folate receptor, as indicated by similar DiO fluorescence intensities in the treated A549 cells (Fig. 2c).

### 3.5. *In vitro* cytotoxicity

The *in vitro* anticancer efficacy of various PTX-loaded nanoparticles against 4T1 cells was assessed using the MTT assay.

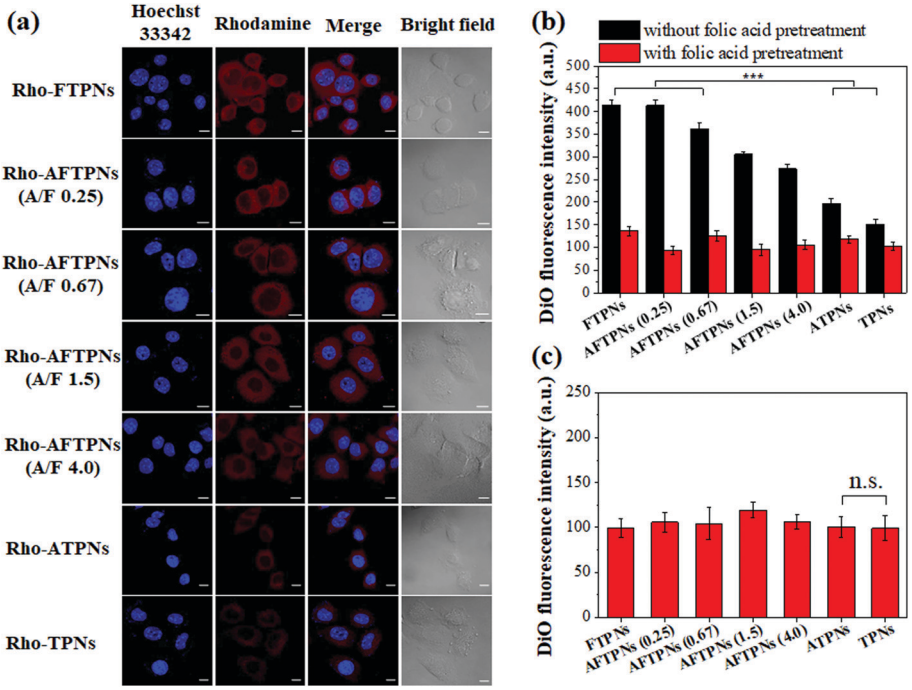


Fig. 2 (a) LSCM images of 4T1 cells treated with various Rho-labeled nanoparticles at 37 °C for 1 h. Scale bars: 10 μm (b) DiO fluorescence intensity of 4T1 cells and folic acid-pretreated 4T1 cells treated with various DiO-loaded nanoparticles (DiO concentration: 10 μM) at 37 °C for 1 h. (c) DiO fluorescence intensity of A549 cells treated with various DiO-loaded nanoparticles (DiO concentration: 10 μM) at 37 °C for 1 h.

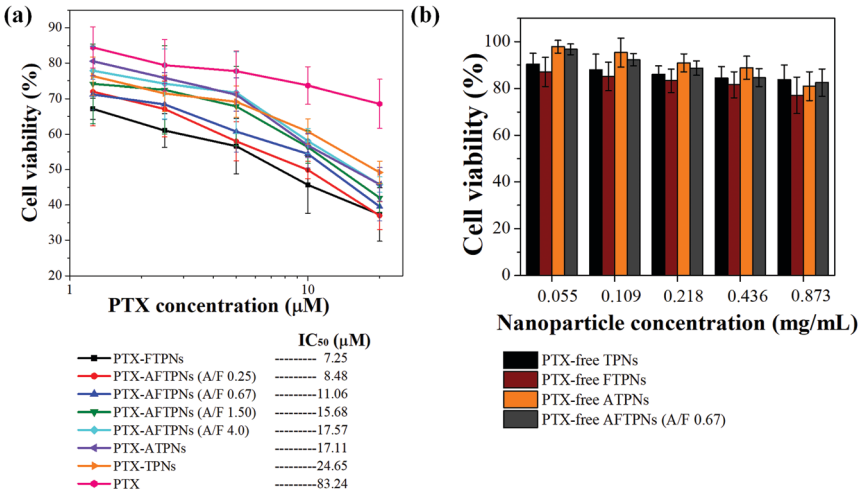


Fig. 3 (a) Cell viability of 4T1 cells treated with free PTX and various PTX-loaded nanoparticles at 37 °C for 8 h. The inset shows the $IC_{50}$ values of free PTX and various PTX-loaded nanoparticles against 4T1 cells. (b) Cell viability of 4T1 cells treated with various PTX-free nanoparticles at 37 °C for 8 h.

4T1 cells were incubated with free PTX and PTX-loaded nanoparticles for 8 h, respectively, followed by an additional 24 h re-incubation to facilitate the drug liberation and the PTX anticancer effect. The viability of treated 4T1 cells was reduced proportionally to the PTX dose from 1.3 to 20 μM (Fig. 3a), while the viability of 4T1 cells treated with PTX-free nanoparticles remained relatively high (Fig. 3b), suggesting that the pristine nanoparticles are essentially noncytotoxic. Moreover, the drug doses required for 50% cellular growth inhibition ($IC_{50}$) by various PTX-loaded nanoparticles were much lower than that (83.2 μM) required for 50% cellular growth inhibition ($IC_{50}$) by free PTX (Fig. 3a and Fig. S13, ESI†). This is ascribed to the enhanced intracellular delivery of PTX *via* endocytic internalization of nanoparticles to cellular microtubules where the therapeutic action of PTX takes place, in contrast to the diffusion-based localization of free hydrophobic PTX largely within cell membranes. More importantly, compared to PTX-ATPNs and PTX-TPNs, the PTX-FTPNs exhibited a significantly lower $IC_{50}$ value, strongly demonstrating that their ability to promote cellular uptake *via* folate receptor-mediated endocytosis considerably enhances the drug cytotoxic effect. Moreover, the $IC_{50}$ values of PTX-AFTPNs with A/F ratios of both 0.25 and 0.67 are comparable to those of PTX-FTPNs, signifying their excellent anticancer performance. Based on the results of the HA binding test, *in vitro* cellular uptake studies and cytotoxicity evaluation, the PTX-AFTPNs with an A/F ratio of 0.67 showed great potential for selectively delivering payloads to bone metastatic regions and folate receptor-overexpressing 4T1 breast cancer *via* their hierarchical dual-targeting property for improved cancer therapy; thus, these nanoparticles were employed in subsequent *in vivo* biodistribution and antitumor studies.

### 3.6. *In vivo* biodistribution study

The dual-targeted effects of AFTPNs on *in vivo* tumor accumulation and biodistribution were further studied using the 4T1 tumor model in female BALB/c mice. TPNs, ATPNs and FTPNs were used as the controls. To clearly examine the biodistribution of these nanoparticles by IVIS, an NIR dye, DiI, instead of PTX lacking pertinent fluorescence properties, was encapsulated into the nanoparticles. At 8 h after intravenous injection with various DiI-containing nanoparticles, the major organs and tibias were isolated from the scarified tumor-bearing mice and examined by IVIS. In contrast to the comparable DiI fluorescence signal intensity in the left tibia and tumor-bearing right tibia of the DiI-loaded TPN group, remarkably enhanced fluorescence signals of the tumor-bearing right tibia compared to the left tibia were observed for the DiI-loaded FTPN, ATPN and AFTPN (A/F = 0.67) groups, particularly for the DiI-loaded ATPN group (Fig. 4a and b). This indicates that ATPNs could efficiently accumulate at bone lesion sites by ALN-mediated bone targeting, whereas FTPNs could reside in the tumor region to some extent *via* tumor folate receptor targeting. For AFTPNs (A/F = 0.67), through dual bone and tumor targeting, their accumulation in bone metastatic regions was evident but was somewhat weaker than that of ATPNs due to the reduced ALN content of the nanoparticle surfaces, which slightly impacts the bone-targeting ability. Statistically insignificant differences of the fluorescence signals among all the NP formulations both in liver and in spleen were observed, indicating similar accumulation of various NPs in both organs.

On the other hand, for tumor-bearing mice treated with various DiI-labeled nanoparticles, the *ex vivo* NIR fluorescence signals of the liver were much higher than those of other organs because of the inevitable uptake of nanoparticles by the reticuloendothelial system (RES) (Fig. 4c and d). Similar biodistributions of nanoparticle-based DDSs in tumor-bearing mice have been extensively reported elsewhere.[30–32]

### 3.7. *In vivo* tumor growth suppression by dual-targeted chemotherapy

To evaluate the *in vivo* antitumor efficacy of various PTX-loaded nanoparticle formulations, the tumor size of the 4T1 tumor-bearing mice was monitored post intravenous injection. In this study, each formulation was applied at a dose of 7.5 mg $kg^{-1}$

 

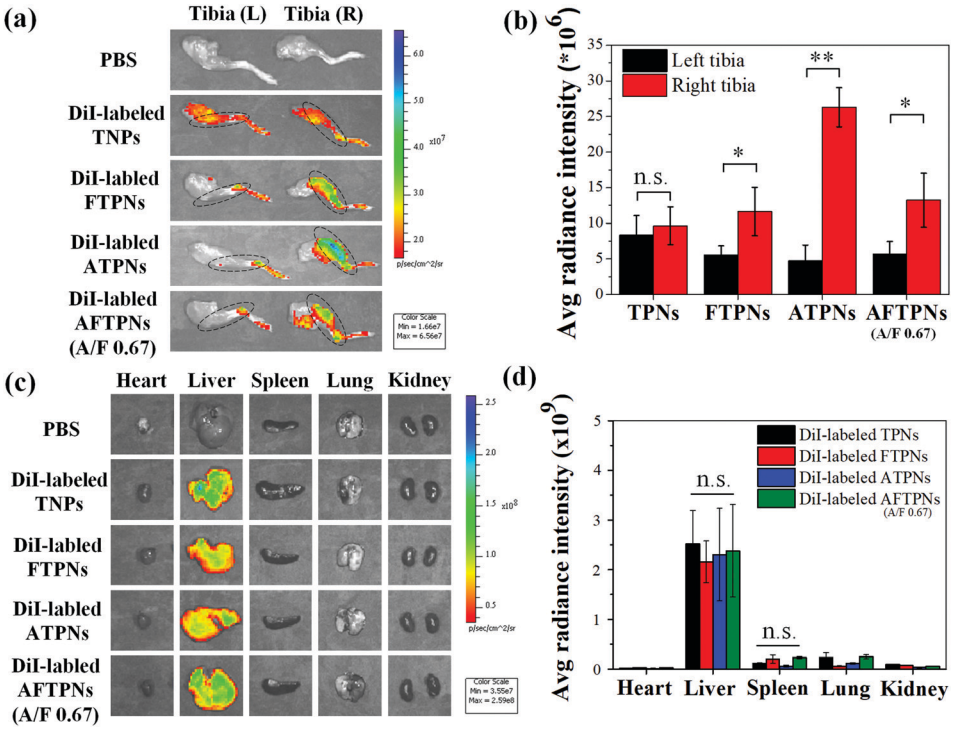


Fig. 4 (a) *Ex vivo* NIR fluorescence images of the isolated tibias of 4T1 tumor-bearing mice at 8 h post injection with PBS and different DiI-labeled nanoparticles. (b) Average DiI fluorescence intensities of the isolated tibias at 8 h post injection with different DiI-labeled nanoparticles. (c) *Ex vivo* NIR fluorescence images of the isolated major organs of 4T1 tumor-bearing mice at 8 h post injection with PBS and different DiI-labeled nanoparticles. (d) Average DiI fluorescence intensities of the isolated organs at 8 h post injection with different DiI-labeled nanoparticles.

PTX, and three doses were given by the tail vein on days 0, 3 and 6. No significant change in the body weights of the treated mice in all groups was observed, suggesting that the formulations adopted in this work did not elicit severe acute toxicity (Fig. 5a). As presented in Fig. 5b, 22 days after treatment, a significant increase in the tumor volume of mice treated with PTX-TPNs was observed, similar to that of the mice treated with PBS. Obviously, the failure to inhibit tumor growth is primarily caused by the poor tumor accumulation of PTX. By contrast, during 22 days of treatment, the administration of PTX-loaded nanoparticles coated with either ALN-TPGS alone, FA-TPGS alone or both ALN-TPGS and FA-TPGS led to remarkable suppression of tumor growth, particularly for PTX-ATPNs and PTX-AFTPNs. More importantly, with an extended time period of 22 to 38 days after the first injection (day 0), compared to the progressively enlarged size of tumors treated with PTX-ATPNs, the tumor size in the mice receiving PTX-AFTPNs remained nearly unchanged (Fig. 5c). These findings strongly confirm that the PTX-AFTPNs exhibit the highest antitumor efficiency by promoting PTX accumulation at bone metastatic sites because of their dual bone/tumor-targeting ability. The median survival of the tumor-bearing mice receiving PTX-AFTPNs was appreciably prolonged ($>50$ days) compared to that of the groups treated with the PTX-ATPNs (35 days), PTX-FTPNs (27 days) and PTX-TPNs (24 days) (Fig. 5d). This further demonstrates the prominent antitumor effect of PTX-AFTPNs that undoubtedly increases the survival rate of the treated mice.

### 3.8. Micro-CT imaging of tibias

The skeletal morphology and BMD of the tibias isolated from the sacrificed tumor-bearing mice after treatment were assessed. As presented in Fig. 6a, compared to the comminuted fractures in the proximal tibias of mice treated with PBS or PTX-TPNs, less destruction was observed in the tibias of mice receiving PTX-FTPNs and PTX-ATPNs. It should be noted that the mice treated with PTX-AFTPNs retained an intact tibia shape comparable to that of the normal mice. Additionally, 2D longitudinal sections and transverse sections of the tibias showed that the tibias in the PBS and PTX-TPN groups were largely damaged, and large pieces of bone fragments were considerably corroded, while the tibias in the PTX-AFTPN group maintained their morphological integrity. In contrast to the significant decline in BMD in the tibias of mice treated with PBS, PTX-TPN, PTX-FTPNs and PTX-ATPNs, an appreciable resistance to the BMD decrease in the tibias of mice receiving PTX-AFTPNs was observed (Fig. 6b). These data suggest that PTX-AFTPNs can effectively prevent the bone destruction and bone loss that frequently occur in association with metastatic bone tumors *via* the dual bone/tumor-targeted delivery of a chemotherapeutic agent.

### 3.9. Safety assessment

To examine the acute side effects of PTX-AFTPNs, histological analysis was conducted by H&E staining of the major organs (heart, liver, spleen, lung and kidney) of sacrificed mice at the treatment endpoint. As illustrated in Fig. 6c, none of the

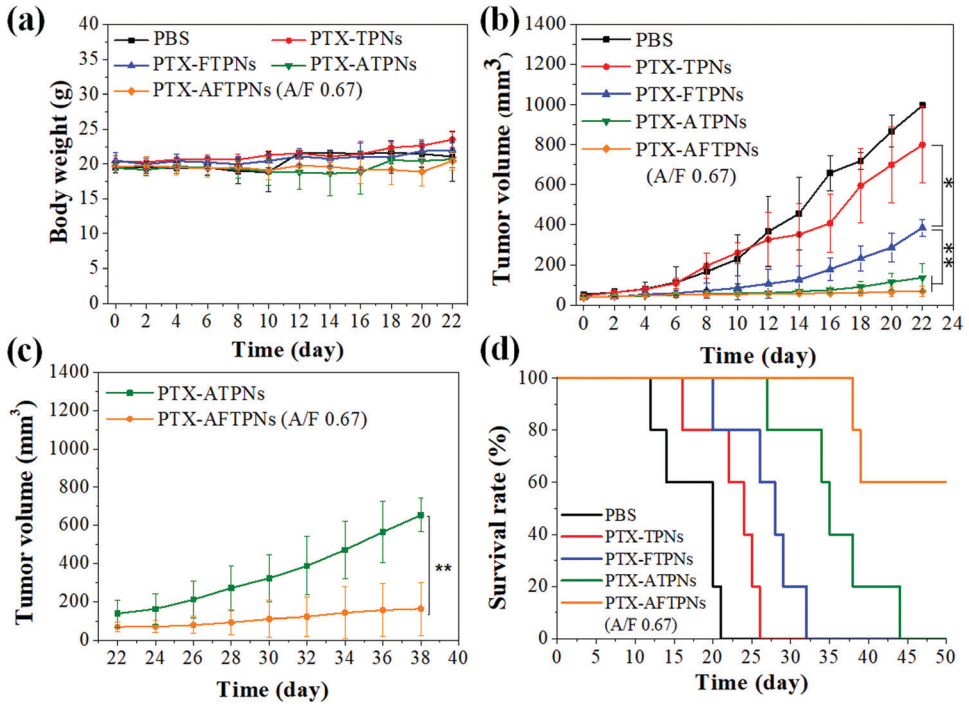


Fig. 5 (a) Body weight of the 4T1 tumor-bearing mice treated with PBS and various PTX-loaded nanoparticles. (b) Tumor growth inhibition profiles of the 4T1 tumor-bearing mice receiving PBS and various PTX-loaded nanoparticles over 22 days after treatment. (c) Tumor growth inhibition profiles of the 4T1 tumor-bearing mice receiving PTX-ATPNs and PTX-AFTPN nanoparticles over an extended time period from day 22 to 38 after treatment. (d) Survival rate of the 4T1 tumor-bearing mice treated with various PTX-loaded nanoparticles.

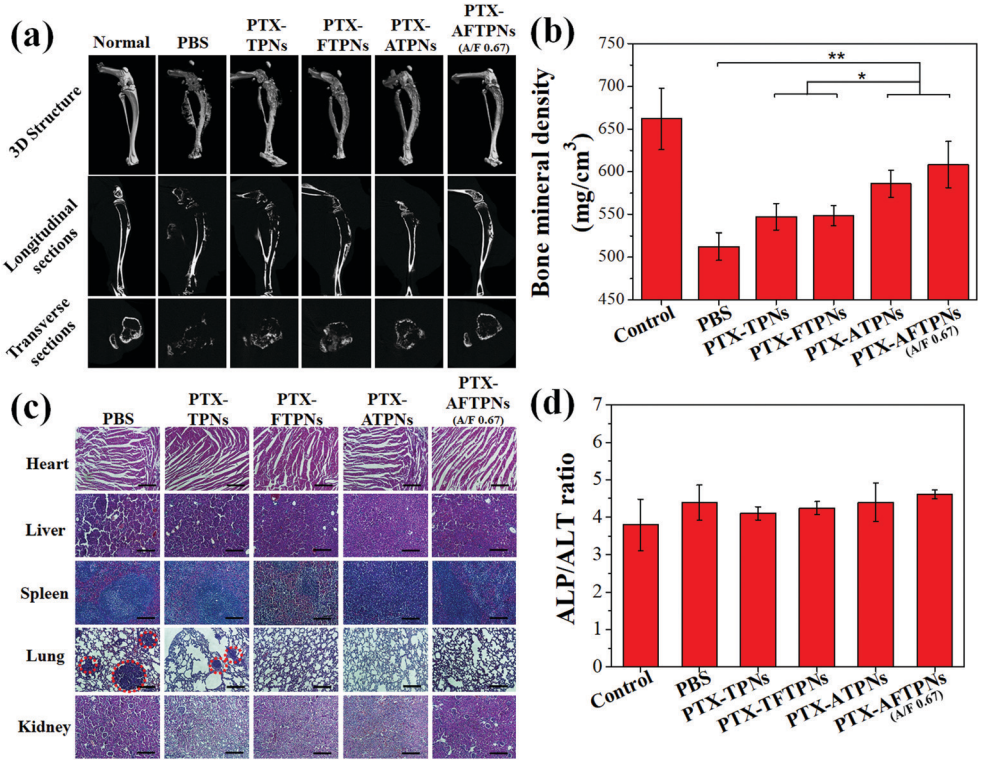


Fig. 6 (a) Micro-CT 3D reconstruction images and 2D images of transverse sections and longitudinal sections of tibias from 4T1 tumor-bearing mice receiving various formulations. (b) Bone mineral density of tibias from 4T1 tumor-bearing mice injected with various formulations. (c) Images of H&E-stained major organs harvested from the 4T1 tumor-bearing mice receiving different treatments. The red circle indicates lung metastatic lesions. Scar bar: 200 μm. (d) Blood biochemical analysis of the mice receiving various treatments on day 14 after the first therapeutic treatment ($n$ = 3). ALT represents the alanine aminotransferase level, and ALP represents the alkaline phosphatase level.

 

treatment groups showed acute adverse effects on the major organs of mice, similar to the PBS group. However, obvious metastatic lung cancer was observed in the PBS and PTX-TPN groups due to the failure to suppress tumor growth and metastasis. By contrast, PTX-ATPNs, PTX-FTPNs and PTX-AFTPNs effectively inhibited lung metastasis by suppressing tumor growth. The liver function of tumor-bearing mice injected with various nanoparticle-based formulations on day 14 after the first therapeutic treatment was assessed. As presented in Fig. 6d, the liver function indices, represented by the ALP/ALT ratio, of the mice receiving various treatments fell into the normal range, ~2 to 4, for healthy mice,[33–35] suggesting that the different PTX-loaded nanoparticles employed in this study do not induce severe hepatic damage. Though a study on the chronic responses to PTX-AFTPNs is required, the current data strongly suggest that the dual-targeted chemotherapy with PTX-AFTPNs developed herein can not only largely avoid side effects on normal tissues but also exert prominent antitumor effects on bone metastatic breast cancer.

## 4. Conclusions

To improve treatment efficacy for bone metastatic breast cancer, a dual bone/tumor-targeted nanoparticle-based delivery system comprising hydrophobic PLGA cores and an ALN-TPGS/FA-TPGS coating was developed to selectively deliver PTX to bone tumor regions. The PTX-loaded AFTPNs not only showed a strong binding affinity for HA but also appreciably enhanced cytotoxicity against folate receptor-overexpressing 4T1 cancer cells by promoting cellular uptake. Notably, the PTX-carrying AFTPNs undergoing dual-targeted delivery to bone and 4T1 tumor cells significantly accumulated in bone metastases *in vivo*, thereby effectively inhibiting 4T1 tumor progression and lung metastasis and increasing the survival rate of the treated mice. Upon treatment, PTX-AFTPNs significantly reduced bone destruction and bone loss while preventing adverse effects on normal tissues. These results demonstrate that the PTX-AFTPN system developed in this work shows great promise for treating bone metastatic breast cancer.

## Conflicts of interest

There are no conflicts to declare.

## Acknowledgements

This work is supported by the Ministry of Science and Technology, Taiwan (MOST 107-2221-E-007-032-MY3 and 108-2314-B-007-004-MY3), National Taiwan University Hospital (107-HCH071) and National Tsing Hua University, Taiwan (108Q2517E1).

## References

1 I. Breuksch, M. Weinert and W. Brenner, *J. Bone Oncol.*, 2016, **5**, 143–145.
2 W. Chu, Y. Huang, C. Yang, Y. Liao, X. Zhang, M. Yan, S. Cui and C. Zhao, *Int. J. Pharm.*, 2017, **516**, 352–363.
3 L. J. Suva, C. Washam, R. W. Nicholas and R. J. Griffin, *Nat. Rev. Endocrinol.*, 2011, **7**, 208–218.
4 K. Miller, C. Clementi, D. Polyak, A. Eldar-Boock, L. Benayoun, I. Barshack, Y. Shaked, G. Pasut and R. Satchi-Fainaro, *Biomaterials*, 2013, **34**, 3795–3806.
5 Y. He, Y. Huang, Z. Huang, Y. Jiang, X. Sun, Y. Shen, W. Chu and C. Zhao, *J. Controlled Release*, 2017, **264**, 76–88.
6 X. Ke, W. Lin, X. Li, H. Wang, X. Xiao and Z. Guo, *Drug Delivery*, 2017, **24**, 1680–1689.
7 T. Yoneda, *J. Orthop. Sci.*, 2000, **5**, 75–81.
8 G. A. Clines and T. A. Guise, *Endocr.-Relat. Cancer*, 2005, **12**, 549–583.
9 T. A. Guise, K. S. Mohammad, G. Clines, E. G. Stebbins, D. H. Wong, L. S. Higgins, R. Vessella, E. Corey, S. Padalecki, L. Suva and J. M. Chirgwin, *Clin. Cancer Res.*, 2006, **12**, 6213–6216.
10 S. B. Bai, D. Z. Liu, Y. Cheng, H. Cui, M. Liu, M. X. Cui, B. L. Zhang, Q. B. Mei and S. Y. Zhou, *Nanomedicine*, 2019, **21**, 102054.
11 L. E. Cole, T. Vargo-Gogola and R. K. Roeder, *Adv. Drug Delivery Rev.*, 2016, **99**, 12–27.
12 S. G. Rotman, D. W. Grijpma, R. G. Richards, T. F. Moriarty, D. Eglin and O. Guillaume, *J. Controlled Release*, 2018, **269**, 88–99.
13 Z. Lei, Z. Mengying, G. Yifei, W. Xiangtao and H. Meihua, *J. Drug Delivery Sci. Technol.*, 2019, **53**, 101133.
14 A. Swami, M. R. Reagan, P. Basto, Y. Mishima, N. Kamaly, S. Glavey, S. Zhang, M. Moschetta, D. Seevaratnam, Y. Zhang, J. Liu and M. Memarzadeh, *et al.*, *Proc. Natl. Acad. Sci. U. S. A.*, 2014, **111**, 10287–10292.
15 Y. Wang, J. Yang, H. Liu, X. Wang, Z. Zhou, Q. Huang, D. Song, X. Cai, L. Li, K. Lin, J. Xiao, P. Liu, Q. Zhang and Y. Cheng, *Biomaterials*, 2017, **114**, 97–105.
16 Q. Chen, C. Zheng, Y. Li, S. Bian, H. Pan, X. Zhao and W. W. Lu, *ACS Appl. Mater. Interfaces*, 2018, **10**, 23700–23710.
17 S. Yamashita, H. Katsumi, N. Hibino, Y. Isobe, Y. Yagi, Y. Tanaka, S. Yamada, C. Naito and A. Yamamoto, *Biomaterials*, 2018, **154**, 74–85.
18 W. L. Ye, Y. P. Zhao, H. Q. Li, R. Na, F. Li, Q. B. Mei, M. G. Zhao and S. Y. Zhou, *Sci. Rep.*, 2015, **5**, 14614.
19 H. Chen, G. Li, H. Chi, D. Wang, C. Tu, L. Pan, L. Zhu, F. Qiu, F. Guo and X. Zhu, *Bioconjugate Chem.*, 2012, **23**, 1915–1924.
20 S. Feng, Z. X. Wu, Z. Zhao, J. Liu, K. Sun, C. Guo, H. Wang and Z. Wu, *ACS Appl. Mater. Interfaces*, 2019, **11**, 7357–7368.
21 X. Ke, W. Lin, X. Li, H. Wang, X. Xiao and Z. Guo, *Drug Delivery*, 2017, **24**, 1680–1689.
22 Y. Xi, T. Jiang, Y. Yu, J. Yu, M. Xue, N. Xu, J. Wen, W. Wang, H. He, Y. Shen, D. Chen, X. Ye and T. J. Webster, *Int. J. Nanomed.*, 2019, **14**, 6425–6437.
23 Q. Chang, R. Geng, S. Wang, D. Qu and X. Kong, *Drug Delivery*, 2016, **23**, 3629–3638.
24 L. Zhao, Y. Zhang, J. Shao, H. Liang, H. Na and J. Zhu, *RSC Adv.*, 2016, **6**, 35658.
25 G. Bansal, J. E. Wright, S. Zhang, R. F. Zernicke and H. Uludag, *J. Biomed. Mater. Res., Part A*, 2005, **74**, 618–628.

26 M. R. Doschak, C. M. Kucharski, J. E. Wright, R. F. Zernicke and H. Uludag, *Mol. Pharmaceutics*, 2009, **6**, 634–640.
27 H. Zhu, H. Chen, X. Zeng, Z. Wang, X. Zhang, Y. Wu, Y. Gao, J. Zhang, K. Liu, R. Liu, L. Cai, L. Mei and S. S. Feng, *Biomaterials*, 2014, **35**, 2391–2400.
28 C. Yang, T. Wu, Y. Qi and Z. Zhang, *Theranostics*, 2018, **8**, 464–485.
29 J. P. van Brussel, G. J. van Steenbrugge, J. C. Romijn, F. H. Schröder and G. H. J. Mickisch, *Eur. J. Cancer*, 1999, **35**, 664–671.
30 C. C. Hung, W. C. Huang, Y. W. Lin, T. W. Yu, H. H. Chen, S. C. Lin, W. H. Chiang and H. C. Chiu, *Theranostics*, 2016, **6**, 302–317.
31 Y. C. Tsai, P. Vijayaraghavan, W. H. Chiang, H. H. Chen, T. I. Liu, M. Y. Shen, A. Omoto, M. Kamimura, K. Soga and H. C. Chiu, *Theranostics*, 2018, **8**, 1435–1448.
32 X. Zhang, R. Zhang, J. Huang, M. Luo, X. Chen, Y. Kang and J. Wu, *J. Mater. Chem. B*, 2019, **7**, 3537–3545.
33 M. Y. Shen, T. I. Liu, T. W. Yu, R. Kv, W. H. Chiang, Y. C. Tsai, H. H. Chen, S. C. Lin and H. C. Chiu, *Biomaterials*, 2019, **197**, 86–100.
34 L. O'Connor, A. W. Harris and A. Strasser, *Cancer Res.*, 2000, **60**, 1217–1220.
35 Z. Y. He, F. Deng, X. W. Wei, C. C. Ma, M. Luo, P. Zhang, Y. X. Sang, X. Liang, L. Liu, H. X. Qin, Y. L. Shen, T. Liu, Y. T. Liu, W. Wang, Y. J. Wen, X. Zhao, X. N. Zhang, Z. Y. Qian and Y. Q. Wei, *Sci. Rep.*, 2016, **6**, 23764.

 